PHYSICS DESIGN OF POLOIDAL FIELD, TOROIDAL FIELD, AND EXTERNAL MAGNETIC DIAGNOSTICS IN KSTAR

BONGJU LEE* *Korea Basic Science Institute, 52 Yeoeun-Dong Taejeon, 305-333, Korea*

NEIL POMPHREY *Princeton Plasma Physics Laboratory, P.O. Box 451 Princeton, New Jersey 08543*

LANG L. LAO *General Atomics, P.O. Box 85608, San Diego, California 92186*

The Korea Superconducting Tokamak Advanced Research (KSTAR) tokamak will have superconducting magnets for both the poloidal field (PF) coils and the toroidal field (TF) coils. The physical arrangement of the PF configuration has 14 coils external to the TF coils. The analysis of the equilibrium flexibility of the KSTAR PF system determines the coil currents required to maintain prescribed equilibrium configurations over the desired range of operational parameters specified for I_p (q_{95}), β_N, and $\ell_i(3)$. Constraints on the plasma separatrix and the flux linkage through the geometric center of the plasma are specified for the free-boundary equilibrium calculations. The ripple magnitude due to the finite number of TF coils and the size of the port for the neutral beam

(NB) injector determine the number, size, and shape of TF coils. Two ripple criteria for a shaped plasma are used for types of ripple transport. The current design of the TF coil, with 16 coils and a D shape, is big enough to satisfy requirements for the ripple magnitude at the plasma and to provide adequate access for tangential NB injection. The external magnetic diagnostics, magnetic probes and flux loops to detect the plasma boundary are designed by the EFIT code, which uses a realistic distributed current source constrained by equilibrium. The proposed configuration with 52 full toroidal flux loops and 78 magnetic probes results in <0.7 cm deviation at critical points, with the Gaussian-distributed 3% random root-mean-square perturbation in the signal.

I. INTRODUCTION

The mission of the Korea Superconducting Tokamak Advanced Research (KSTAR) project[1] is to develop a steady-state-capable advanced superconducting tokamak to establish a scientific and technological basis for an attractive fusion reactor. In this context, the research objectives have been established as follows: to extend the present stability and performance boundaries of tokamak operation through active control of profiles and transport; to explore methods to achieve steady-state operation for tokamak fusion reactors using noninductive current drive; and to integrate optimized plasma performance and continuous operation as a step toward an

attractive tokamak fusion reactor. To meet the mission and research objectives, the design of the KSTAR tokamak features fully superconducting magnets, long-pulse operation capability, flexible pressure and current profile controls, flexible plasma shape and position control, and advanced profile and control diagnostics.

The KSTAR tokamak will function both as a versatile test bed and as a development tool for advanced tokamak regimes with reasonably long sustainment time, taking advantage of a fully superconducting magnet system. A number of the high-performance operational scenarios being studied in today's tokamaks, such as the H mode, negative central shear (NCS) mode, and high-ℓ_i mode, can be further studied in KSTAR with its substantial heating and current drive capabilities and its flexible poloidal field (PF) system. An outboard passive
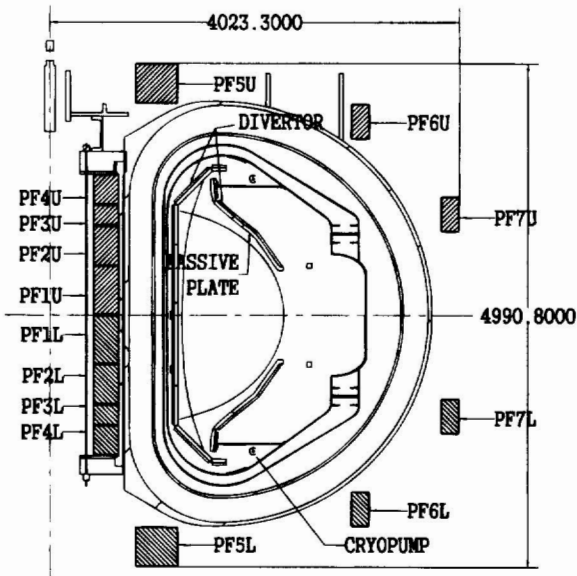
*E-mail: bjlee@kstar.kbsi.re.kr

Fig. 1. Configuration of PF coil and TF coil in KSTAR, showing the double-wall vacuum vessel, passive plate for vertical stability, internal coils for active control, divertor, and cryopump. The separatrix is shown inside the passive plate.

structure close to the plasma contributes to the plasma stabilization.

The design points of major tokamak parameters are defined as follows: machine size ($R_0 = 1.8$ m, $a = 0.5$ m), performance ($B_{T_0} = 3.5$ T, $I_p = 2.0$ MA), plasma shape ($\kappa = 2.0$, $\delta = 1.8$, double-null divertor), current drive and heating power (initial $P_{heat} = 15.5$ MW, upgradable to 27.5 MW), and pulse length (initial $\tau_{pulse} = 20$ s, final $\tau_{pulse} = 300$ s with upgraded power handling system). KSTAR will have a PF system capable of providing a flux swing of 15.5 Wb (volt-seconds) to allow full inductive operation for an ~20-s flattop. With su-

superconducting toroidal field (TF) and PF coils and non-inductive current drive, it will be capable of true steady-state operation.

Among seven PF coil pairs, which are up-down symmetric, the central solenoid consists of four pairs of modules (PF1 through 4) to provide mainly a flux swing and some shaping capability. In addition, there is a pair of divertor coils (PF5) and two pairs of outboard ring coils (PF6 and 7). The seven-coil-pair arrangement (see Fig. 1) has the ability to provide a pure Ohmic distribution so the plasma shape can be held fixed during an inductively maintained flattop. The PF coil centroid locations were scaled from their locations in the Tokamak Physics Experiment (TPX) design,[2] where a detailed optimization was performed. The aspect ratios for the individual coils were chosen equal to the values assumed for TPX. Table I summarizes the specification of each PF coil.

From a plasma physics point of view, the ripple component of the toroidal field due to the finite number of the TF coils should be considered in the design of TF coils since ripple on field may result in rapid loss of energetic ions. Besides ripple, the mechanical configuration of the TF coils affects the accessibility of the tokamak and must be considered.

The two classes of energetic particles to be considered for KSTAR plasmas are neutral beam (NB) ions and ion cyclotron resonance heating (ICRH)-tail ions. Fusion-born energetic ions are not required to be well confined in KSTAR. The NB ions are expected to be below 120 keV, and the ICRH minority ions can be above 1 MeV. The most energetic part of these ions will have an anisotropic pitch angle distribution, but they can become more isotropic as they slow down and scatter in pitch angle. A nonnegligible fraction of the energetic ions can then be subject to ripple-trapped and/or collisionless stochastic losses.

KSTAR shape control on the slow timescale (≥ 100 ms) will use PF coils to control a small number of critical plasma shape and flux parameters in the

TABLE I

PF Coil Specifications

Coil	R_c (m)	Z_c (m)	ΔR_c (m)	ΔZ_c (m)	Turns
PF1U(L)	0.544	±0.243	0.2265	0.4854	180 (180)
PF2U(L)	0.544	±0.694	0.2265	0.3810	144 (144)
PF3U(L)	0.544	±0.997	0.2265	0.1898	72 (72)
PF4U(L)	0.544	±1.252	0.2265	0.2854	108 (108)
PF5U(L)	1.043	±2.296	0.3936	0.3808	256 (256)
PF6U(L)	3.044	±1.920	0.1546	0.3330	84 (84)
PF7U(L)	3.926	±1.000	0.1546	0.3330	84 (84)

magnetic field geometry based on measurements of flux and their derivatives. Flux values from full-flux loops provide the starting point for the extrapolation of flux values to the plasma boundary. Magnetic probes, both close to the flux loops and close to the plasma, provide the values for the flux derivatives, which allow an accurate extrapolation. The reconstruction of the plasma boundary is examined using a fast magnetostatic algorithm with distributed current source[3] to assess the importance of measurement locations and their quality. In addition to the plasma shape and the sum of β_p and $\ell_i/2$ (β_p and ℓ_i separately for sufficiently elongated plasmas), this method also yields a current profile consistent with magneto-hydrodynamic (MHD) equilibrium constraints. In this paper, we focus on the evaluation of the proposed configuration for probes and loops by the KSTAR diagnostic group and seek possible modifications based on identifying the influential location of probes and loops with the minimum numbers.

This paper is organized as follows. In Sec. II, we discuss the design basis for the PF coils. In Sec. III, the physics basis for designing the TF coil is presented. The method and results for magnetic probes and flux loops are discussed in Sec. IV. Conclusions are presented in Sec. V.

II. FLEXIBILITY OF KSTAR PF SYSTEM

Configuration flexibility is an important element of the KSTAR design approach. We have attained flexibility in the design by demonstrating the ability to accommodate a wide range of plasma parameters. The equilibrium flexibility of the KSTAR PF system is examined using the Tokamak Simulation Code[4] free-boundary MHD equilibrium feature, which solves the Grad-Shafranov equation for chosen plasma shape constraints and plasma profiles.

The primary purpose of these analyses is the determination of the PF coil currents required to maintain prescribed equilibrium configurations over the desired range of operational parameters, usually specified in terms of the plasma current I_p (q_{95}), normalized toroidal beta β_N ($\equiv \beta(\%)[a \, (m) \, B_T \, (T)]/[I \, (MA)]$), and normalized plasma internal inductance $\ell_i(3)(\equiv(2V\langle B_p^2\rangle)/[(\mu_0 I_p)^2 R_0])$, where V is the plasma volume and $\langle B_p^2\rangle = \int B_p^2 \, dV/\int dV$ is the volume average of the square of the poloidal magnetic field.

The reference operating mode of KSTAR is characterized by parameter values of $I_p = 2$ MA and $\beta_N = 3.5$ with the standard monotonically increasing safety factor q profile. A programmed inductive plasma initiation sequence uses electron cyclotron heating to facilitate breakdown and current buildup. Starting from the time of breakdown with at least 6-V loop voltage in the absence of plasma, the plasma current increases 100 kA within

0.3 s. The inductive mode evolves such that the plasma current is ramped from 100 kA to a flattop maximum of 2 MA in 4 s. Auxiliary heating is then applied to increase β. With the assumed energy confinement time of $\sim$1.8 s, the auxiliary heating power of 27 MW is necessary to get the target value of $\beta_N = 3.5$ or $\beta = 4\%$ at $B_T = 3.5$ T. The flattop phase is sustained over 20 s, and then the plasma current is ramped down to zero in 4 s, while the auxiliary heating power is gradually turned off.

To determine the initial flux bias, superconductor limits on fraction of critical current density, current density in the copper stabilizer, heat transfer rate for a recovery event, and temperature headroom of the superconductor are analyzed for configurations of PF coil currents that satisfy the shape constraints but differ in plasma flux linkage by 1 Wb. The volt-second consumption during the current ramp-up phase can be estimated in a spreadsheet level. The fluxes generated by PF coils can be divided into an external piece, corresponding to the flux through a toroidal strip between machine axis and the inside edge of the plasma, and an internal piece, corresponding to a strip between the inside edge of the plasma and the magnetic axis. Spreadsheet-level estimates of external inductive flux contribution are conveniently provided by the analytic expressions,[5] which are numerical fits to the exact external inductance of elliptical plasmas of varying aspect ratio. The internal piece of flux consists of the inductive contribution, which is expressed as $0.5\mu_0 R\ell_i I_p$, and the resistive contribution. The database shows that minimum resistive losses during ramp-up can be fit empirically to the form $\Delta\Psi_{res} = C_E\mu_0 R_0 I_p$, where C_E, the Ejima coefficient,[6] has the value $C_E \approx 0.4$ and strongly depends on the ramp-up time. Estimated values[7] of flux consumption for the KSTAR operating modes are 13.65 Wb for the baseline operating mode, 12.83 Wb for the low-ℓ_i ($= 0.4$) mode, and 15.28 Wb for the high-ℓ_i ($= 1.3$) mode. In Ejima's calculation, C_E is assumed to be 1 for up to 100-kA plasma current and 0.65 for up to 2-MA plasma current during the ramp-up period. These values are larger than the experimentally deduced value of 0.4 because it is the voltage limitation on the PF coils instead of the development of skin currents that sets the minimum current ramp-up time. These are calculated based on the scenario of a 4.4-s rampup and a 20-s flattop.

II.A. Equilibrium Description

The equilibrium analyses utilize a variety of profile forms for pressure and TF function $g(= RB_t)$ to represent nominal and extreme ranges of plasma operation by solving the Grad-Shafranov equation

$$\Delta^*\psi_p = -(8\pi^2 R/c)J_t(R,\psi) , \qquad (1)$$

where

$$J_t = 2\pi cR[p'(\psi) + g^{2'}(\psi)/2\pi c^2 R^2] . \qquad (2)$$

The nominal profiles have the following forms for the plasma pressure and g:

$$\frac{p(\psi)}{p(0)} = (1 - \hat{\psi})^{\alpha_p} \quad (3)$$

and

$$g^2 = (R_0 B_{0T})^2 + 2[-c_{g1}\hat{\psi}^{\alpha_g} - 4c_{g2}(1 - \hat{\psi})] \,, \quad (4)$$

where $\hat{\psi} = (\psi_{lim} - \psi)/(\psi_{lim} - \psi_{min})$ is the normalized poloidal flux. The desired β_N is obtained by adjusting $p(0)$. Typical values of the pressure and TF function shape parameters are $\alpha_p = 2.0$ and $\alpha_g = 2.0$. The parameters c_{g1}, c_{g2}, and α_g in the TF function are adjusted to yield the desired values of ℓ_i and I_p. Figure 2 shows the pressure and current density profiles of a typical baseline discharge of KSTAR.

II.B. Plasma Operating Space and Constraints

Free-boundary equilibria have been generated to assess the ability of the KSTAR PF system to produce equilibria satisfying all the shape constraints for plasma profiles in the range $1.5 \leq \beta_N \leq 5$ and $0.4 \leq \ell_i \leq 1.3$ for steady state. Also, start-up reference equilibria with $\beta_N = 0.3$ and $0.8 \leq \ell_i \leq 1.2$ can be produced. We have also verified that double-null (DN) configurations with high edge safety factor $q_{95} > 5$ at $\beta_N = 5$ are possible.

The 14 PF coils are connected in an up-down symmetric configuration of seven independent circuits (PF1U+L, PF2U+L, PF3U+L, PF4U+L, PF5U+L, PF6U+L, and PF7U+L) for DN equilibria. For the DN analyses, there are typically three hard geometric constraints on the plasma separatrix, namely, specified values for the inboard and outboard midplane radii ($R \pm a$

at $Z = 0$) and a specified location for the separatrix strike point on the divertor plate. The flux linkage through the geometric center of the plasma is also specified, which means there are four strict constraints among the seven independent coil groups. The remaining three degrees of freedom are used to position the X point so that the scrape-off-layer (SOL) surface that is 2 cm from the separatrix on the midplane does not intersect any material surfaces other than the divertor, to maintain sufficient elongation to satisfy $q_{95} > 3$, and to regularize the coil current distribution by minimizing the sum of the coil current densities $\sum_{j=1}^{ncoil}(I_j/\Delta A_j)^2$. Table II is the summary of the PF coil currents at two startup and four steady-state operating corners. Note that I_p was lowered for the $\ell_i = 1.3$ and $\beta_N = 5$ case to satisfy the high-q_{95} (>5) constraint.

In the explicitly up-down symmetric current connections of DN plasma in KSTAR, the vertical instability is inherent. This mode predominantly involves axisymmetric rigid vertical motion of the entire plasma ($n/m = 0/1$). Since the growth time of the axisymmetric mode is the poloidal Alfven timescale ($\sim \mu s$), a conducting structure must be located close enough to the plasma to slow down the plasma motion by the radial magnetic field induced by the eddy current. Then, an active control system must be incorporated to compensate for the resistive decay of the passive structure currents and allow us to maintain the plasma on the midplane indefinitely. Figure 1 shows both the passive plate and internal coil set, which is made of copper, for an active control.

The PF coils for single-null (SN) operation are connected into nine independently controllable circuits with PF1U+L, PF2U+L, PF3U+L, PF4U+L, PF5U, PF5L, PF6U, PF6L, and PF7U+L. The geometric constraints on SN plasmas are the same as on DN plasma, but in
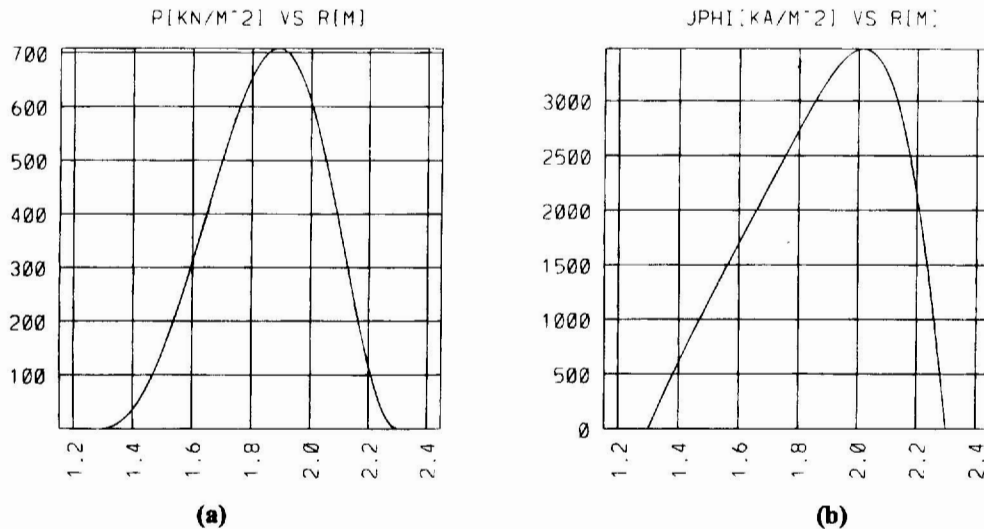

Fig. 2. (a) Pressure and (b) current density profiles of the baseline discharge of KSTAR. The elongation and triangularity of plasma for this discharge are 2.0 and 0.8, respectively ($\beta_N = 3.5$ or $\beta = 4\%$ at $B_T = 3.5$ T and $\ell_i = 0.8$).

TABLE II

Coil Currents and Flux Linkages for Six Flexibility Equilibria

	Startup		Steady-State Flexibility			
β_N	0.3	0.3	1.5	1.5	5	5
$\ell_i(3)$	0.8	1.2	0.4	1.3	0.4	1.3
I_p	2 MA	2 MA	2 MA	2 MA	2 MA	1.2 MA
Flux linkage	3	3	6	6	6	6
I_PF1(kA-turn)	−1755	−3019	−859	−3899	−894	−2491
I_PF2(kA-turn)	−1144	180	−5240	418	−3681	−666
I_PF3(kA-turn)	672	552	−74	160	16	−321
I_PF4(kA-turn)	2987	1740	2740	105	1866	−844
I_PF5(kA-turn)	2967	1943	2640	1548	3475	−248
I_PF6(kA-turn)	−1123	−158	−2430	−310	−2536	344
I_PF7(kA-turn)	−452	−1149	283	−1227	58	−1372

addition the inactive separatrix must be outside the SOL that is 2 cm from the separatrix on the midplane. Table III has the same information as Table II, but for SN plasmas. High-ℓ_i cases also have reduced I_p to satisfy the $q_{95} > 3$ constraints.

III. KSTAR TF COIL DESIGN

Axisymmetry of magnetic field topology is necessary for good classical particle confinement. However, due to discreteness of the TF coil system, it is unavoidable to have some ripple component in the toroidal magnetic field. This can allow rapid loss of energetic ions. The ripple strength $\delta \equiv (B_{max} - B_{min})/(B_{max} + B_{min})$ is a function of position. The TF coils must be designed to limit the loss of NB-injected energetic particles caused by ripple.

The ripple requirement, which must be <0.20% over the plasma cross section of KSTAR to avoid energetic particle loss, can give design requirements on size, shape, and number of TF coils. Two types of ripple losses are considered in the KSTAR design: ripple trapping (RT) and collisionless stochastic ripple (CSR) losses. Collisional effects are neglected at this stage of the design phase.

III.A. Ripple-Trapping Loss

Weakly collisional, energetic particles can be trapped in the local ripple well if their perpendicular (to B) energy

TABLE III

Coil Currents and Flux Linkage at Four Steady-State Operating Corners of SN Plasma

	Steady-State Flexibility			
β_N	1.5	1.5	5	5
$\ell_i(3)$	0.4	1.3	0.4	1.3
I_p	2 MA	1.75 MA	2 MA	1.75 MA
Flux linkage	6	6	6	6
I_PF1U(kA-turn)	−2030	−3800	−1540	−2930
I_PF2U(kA-turn)	−2960	271	−2400	369
I_PF3U(kA-turn)	−47	26	53	−179
I_PF4U(kA-turn)	1380	−254	1080	−95
I_PF5U(kA-turn)	1690	−726	1850	−171
I_PF6U(kA-turn)	−1590	845	−1240	847
I_PF7U(kA-turn)	8	−1370	−561	−1760
I_PF3L(kA-turn)	−47	26	53	−179
I_PF4L(kA-turn)	1380	−254	1080	−95
I_PF5L(kA-turn)	3410	1590	2930	773
I_PF6L(kA-turn)	−2430	−432	−1710	37

is much higher than the parallel energy. The ripple-trapped particles can then be lost rapidly by ∇B drift motion. ICRH-tail ions or NB ions can be pitch-angle scattered into the ripple-trapping region as they slow down.

The local magnetic ripple well is usually maximal around the outside midplane, $\theta = 0$ deg. However, $\theta = 0$ deg is not a good place to study a ripple-trapping requirement because any nonzero ripple value gives a local ripple well there, which may well be of measure zero. As is now common in machine design studies, $\cos \theta = 0.8$ is chosen as a good reference place[8] to configure the requirement against ripple trapping:

$$\delta < \delta_t = \frac{a}{NqR} \frac{\sin \theta [(1 + \kappa^2)/2]^{1/2}}{(\sin^2 \theta + \kappa^2 \cos^2 \theta)^{1/2}} \ , \qquad (5)$$

where

  a = horizontal minor radius

  N = number of TF coils

  q = safety factor

  R = major radius

  κ = elongation factor.

When we apply this condition on the ψ_{95} surface, Eq. (5) gives $\delta_t = 0.195\%$ for the nominal plasma ($\kappa = 2$) of KSTAR.

III.B. Collisionless Stochastic Ripple Loss

The nonaxisymmetric ripple field induces stochastic radial motion of trapped ions when the ion energy exceeds a critical value characterized by the ripple strength at the banana tip. A reasonable upper limit against CSR loss of energetic ions can be obtained by requiring that the ions turning at $\theta = 90$ deg are below the CSR loss threshold. By modifying the formula of Goldston et al.[9] to include the effect of elongation and triangularity, we have[10]

$$\delta < \delta_s \approx \frac{\kappa}{\sin \alpha} \left(\frac{a}{\pi R N q} \right)^{3/2} \frac{0.6}{\rho q'} \ , \qquad (6)$$

where

  ρ = gyroradius of the energetic ion

  α = angle between the flux surface and the vertical line at $\theta = 90$ deg

  q' = radial derivative of the safety factor.

The required ripple strength for the stochastic loss is inversely proportional to the particle speed. Equation (6) gives $\delta_s = 0.01\%$ for 1-MeV ICRH-tail (hydrogen) minority ions, the occurrence of which is rare, and $\delta_s = 0.055\%$ for the partially slowed-down beam ions at 80 keV of KSTAR.
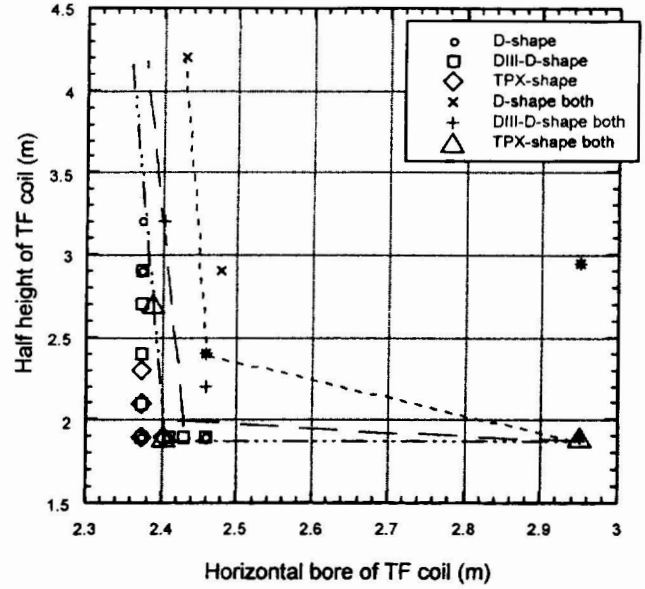

Fig. 3. Horizontal bore plotted against height, showing that the TPX shape requires the smallest TF coil against particle loss due to ripple.

A series of calculations of the ripple due to various possible TF magnet designs was performed. Three different TF shapes were considered; D shape, DIII-D shape (angled D), and TPX (racetrack) shape. The cases of 16 and 12 TF coils were also considered with their different sizes. The AV8 code, which is based on Ref. 11 and treats each TF coil as a toroidal array of filaments, was used for calculations. This code evaluates the magnetic field and magnetic vector potential and their derivatives for the current-carrying straight wire of finite length and the current-carrying closed polygon (not necessarily plane) consisting of three or more wires of finite length.

The region of the right-hand and upper sides of lines in Fig. 3 basically represents the height and width of a TF coil that can satisfy $\delta_t < 0.5\%$ at the position of $R = 2.31$ m and $Z = 0.02$ m, and $\delta_s < 0.03\%$ at the position of $R = 1.81$ m and $Z = 0.75$ m. Lines connect the points at each TF shape at which both criteria are satisfied. Points not labeled "both" satisfy either only one or none of the criteria. The TPX shape gives the smallest TF coils. Overall, the TF coil shape strongly affects δ. Another observation is that δ_t is more sensitive to TF width than height, and δ_s is more sensitive to TF height than width. Figure 3 shows that the 12-coil TPX shape, the size of which is the same as the current design, does not satisfy the criterion for RT loss even though it requires the smallest coils among three different coil shapes. Additional works[10] show that both criteria, $\delta_t < 0.5\%$ at the position of $R = 2.31$ m and $Z = 0.02$ m, and $\delta_s < 0.03\%$ at the position of $R = 1.81$ m and $Z = 0.75$ m, cannot be satisfied with any shape of 12 coils.

The current design of the KSTAR TF coils have a horizontal bore of 2.36 m, a height of 3.53 m (measured

from the center of the TF winding pack), and a winding pack cross section of height 0.22 m and width 0.27 m. The TF coils generate ripple strengths of $\delta_T = 0.084\%$ and $\delta_S = 0.026\%$ compared to design criteria of $\delta_T < 0.195\%$ and $\delta_S < 0.055\%$. Figure 3 demonstrates that from the point of view of ripple losses, KSTAR can have smaller TF coils. The current design, however, is determined by other requirements such as the dimensions of the NB injector ports, and manufacturing requirements such as the curvature of superconducting elements.

IV. DESIGN OF EXTERNAL MAGNETIC DIAGNOSTICS

Important characteristics of the discharge shape include the number and location of X points, the distance between the last closed flux surface and the vacuum vessel walls, the elongation, triangularity, the major and minor radii, and the location where the divertor separatrix flux surface strikes the vessel wall. These characteristics influence tokamak performance in areas such as MHD stability properties, the location where the heat lost from the discharge is deposited on the vessel wall, whether the vertical position can be controlled, and the loading resistance for radio-frequency heating antennas.

The task of the equilibrium reconstruction algorithm discussed here is to compute the distributions in the R, Z plane of the poloidal flux (ψ) and the toroidal current density (J_t) that provide a least-squares best fit to diagnostic data and which simultaneously satisfy the model given by the Grad-Shafranov equation, Eq. (1).

The current in EFIT code[12] is modeled as being distributed among a configuration of rectangular elements, one centered at each grid point, with the total number of grid points typically 1000 or more. The large number of grid points allows the solution to provide a realistic distribution of the current density, including provision for finite current density at the discharge edge. EFIT interleaves the equilibrium and the fitting iterations to find the optimum solution, which retains the computational efficiency of the filament current fitting method,[13] but improves on the accuracy. The two free functions $P'(\psi)$ and $g^{2'}(\psi)$ in J_t are modeled as polynomials in ψ, with linear coefficients to be determined from the measured signals and the imposed constraints.

Standard procedures[14] to determine the number and position of magnetic probes and flux loops are as follows:

1. Put a large number of magnetic probes and flux loops around the plasma vessel at the position where they are likely to be built.

2. Run EFIT in equilibrium mode to compute magnetic signals at these probes and flux loops for various plasma shapes and configurations of interest.

3. Use these simulated signals as input to do a reconstruction using EFIT and compare reconstructed equilibrium to the original.

4. Perturb signals by 3% randomly and run reconstruction for a large number of cases to determine the accuracy of reconstruction for this particular configuration of magnetic probes and flux loops.

5. Optimize locations and number of magnetic probes and flux loops by adding or removing magnetic probes and flux loops as well as changing their locations.

In these serial calculations, eddy current on the passive plate and vacuum vessel is not considered. Three different plasma profiles are considered: L-mode profiles, H-mode profiles characterized by finite edge pressure gradient and edge current, and NCS profiles characterized by a hollow current profile.

The sum of the squares (χ^2) of the difference between reconstructed and measured signals normalized by the statistical error and the condition number cno, which is the ratio between the first and last eigenvalues of the response matrix and the measure of the robustness of fit, have been monitored for proper locations of loops and probes. For large cno, small changes in the data can result in large changes in the solution. Only well converged runs are selected in Tables IV through VII. There is not enough information for the code to extrapolate the necessary flux information around the computational grid if the code proceeds with an insufficient number of loops and probes. Critical points such as $R - a$, $R + a$, the X point, and the striking point are compared with ones in the targeted equilibrium to provide a quantitative comparison. Additive 3% Gaussian-distributed random perturbations in the signal to loops and probes are applied for the simulation of the real experimental situation.

Configuration (a) in Fig. 4 was proposed by the KSTAR diagnostics group for the reference numbers and position of 52 full toroidal flux loops and 78 magnetic probes. The diagnostics group claims that these are the maximally affordable numbers of probes and loops inside the vacuum vessel. Since the field varies steeply near the X points compared to other areas, eight probes are relocated just behind the outboard divertor, i.e., configuration (b). Configuration (d), which has 28 full toroidal flux loops and 40 magnetic probes, was obtained by a systematic approach[15] based on flux and field patterns generated by plasma along the measurement contour, which could identify some critical points to reconstruct equilibrium properly. To see the effect due to the probes behind the divertor, configuration (c) is considered.

We impose a 3% error in the signal because integrators to measure signals from magnetic probes and flux loops are always subject to errors. This 3% error may be too large for the future digital integrator, but

TABLE IV

Deviation* at Reference Points from the Target Equilibrium with Configuration (a) in Fig. 4

L Mode	Test Positions						Code Diagnostics	
	$R - a$	$R + a$	Upper X Point	Lower X Point	UISP[a]	UOSP[b]	χ^{2c}	cno^d
Without error 3% error	0.05 0.11	0.21 0.76	0.50 0.57	0.50 0.66	0.31 0.78	0.60 0.47	3.5 19	4.25E5[e] 4.5E5
H Mode								
Without error 3% error	0.34 0.38	0.43 0.49	0.45 0.69	0.64 0.51	0.31 0.51	0.24 0.42	0.26 18	8.9E5 9.0E5
NCS Mode								
Without error 3% error	0.01 0.10	0.01 0.32	0.14 0.36	0.14 0.45	0.01 0.22	0.01 0.25	0.00 13	9.1E6 5.2E6

*In centimetres.
[a]UISP = upper inboard strike point.
[b]UOSP = upper outboard strike point.
[c]χ^2 = sum of the squares of the difference between the reconstructed probe and loop values and their measured values, normalized by the statistical error.
[d]cno = condition number.
[e]Read as 4.2×10^5.

TABLE V

Deviation* at Reference Points from the Target Equilibrium with Configuration (a) in Fig. 4

L Mode	Test Positions						Code Diagnostics	
	$R - a$	$R + a$	Upper X Point	Lower X Point	UISP[a]	UOSP[b]	χ^{2c}	cno^d
Without error 3% error	0.08 0.14	0.20 0.68	0.45 0.31	0.32 0.51	0.28 0.58	0.36 0.27	2.1 15	2.9E5[e] 2.9E5
H Mode								
Without error 3% error	0.29 0.33	0.59 0.48	0.22 0.65	0.58 0.30	0.35 0.21	0.22 0.28	0.44 18	8.4E5 8.3E5
NCS Mode								
Without error 3% error	0.09 0.12	0.12 0.27	0.14 0.50	0.14 0.28	0.09 0.01	0.11 0.04	0.44 14	7.2E5 4.4E6

*In centimetres.
[a]UISP = upper inboard strike point.
[b]UOSP = upper outboard strike point.
[c]χ^2 = sum of the squares of the difference between the reconstructed probe and loop values and their measured values, normalized by the statistical error.
[d]cno = condition number.
[e]Read as 2.9×10^5.

TABLE VI

Deviation* at Reference Points from the Target Equilibrium with Configuration (b)

L Mode	R − a	R + a	Upper X Point	Lower X Point	UISP[a]	UOSP[b]	χ^{2c}	cno[d]
Without error	0.05	0.21	0.50	0.58	0.54	0.51	0.01	6.6E6[e]
3% error	0.15	0.56	0.63	0.87	1.06	1.95	5.5	2.7E5
H Mode								
Without error	0.30	0.31	0.20	0.20	0.06	0.13	0.19	9.2E5
3% error	0.70	1.27	1.39	0.31	0.29	0.25	7	9.4E5
NCS Mode								
Without error	0.05	0.07	0.10	0.10	0.03	0.05	0.07	8.4E5
3% error	0.73	1.13	0.99	1.03	0.21	0.21	5	8.8E5

*In centimetres.
[a]UISP = upper inboard strike point.
[b]UOSP = upper outboard strike point.
[c]χ^2 = sum of the squares of the difference between the reconstructed probe and loop values and their measured values, normalized by the statistical error.
[d]cno = condition number.
[e]Read as 6.6×10^6.

TABLE VII

Deviation* at Reference Points from the Target Equilibrium with Configuration (c)

L Mode	R − a	R + a	Upper X Point	Lower X Point	UISP[a]	UOSP[b]	χ^{2c}	cno[d]
Without error	0.02	0.34	0.14	0.14	0.05	0.09	0.47	4.9E5[e]
3% error	0.11	0.57	0.74	0.71	0.50	0.97	6.2	3.9E5
H Mode								
Without error	0.25	0.82	0.58	0.28	0.09	0.25	0.02	9.8E5
3% error	0.21	0.64	0.79	0.88	1.26	0.65	6	9.9E5
NCS Mode								
Without error	0.07	0.09	0.10	0.10	0.08	0.18	0.02	7.9E5
3% error	0.14	0.37	1.32	1.10	0.54	1.16	5.7	6.8E5

*In centimetres.
[a]UISP = upper inboard strike point.
[b]UOSP = upper outboard strike point.
[c]χ^2 = sum of the squares of the difference between the reconstructed probe and loop values and their measured values, normalized by the statistical error.
[d]cno = condition number.
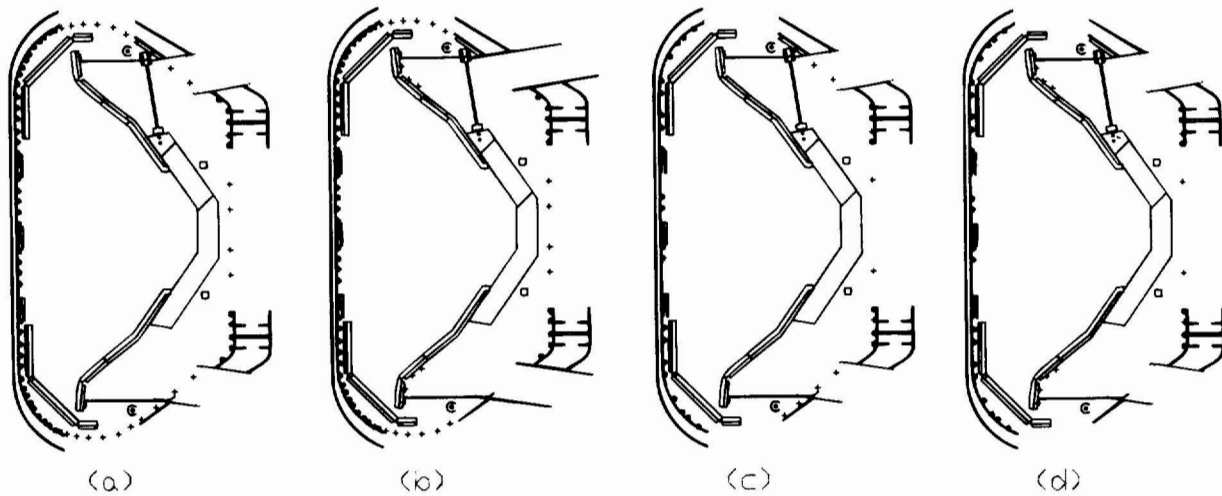[e]Read as 4.9×10^5.

Fig. 4. Four different configurations for flux loops and magnetic probes. The circles and the pluses represent flux loops and magnetic probes, respectively.

it is necessary to test the reliability of the KSTAR magnetic diagnostics in such large perturbations. The errors in a digital integrator are caused by transients that occur in a time shorter than the sampling interval. The χ^2 in Tables IV through VII is larger in cases with a random perturbation in the signal and many loops and probes. Therefore, a lower χ^2 is not necessary for better reconstruction. Based on results, $\chi^2 < 20$ and a condition number $<1.0 \times 10^7$ are required to get a good fit.

Configuration (c) gives the largest deviation among the four configurations in general. The probes behind the outboard divertor do not have much effect on the quality of reconstruction with configurations (a) and (b) because of their many loops and probes, but they do affect configurations (c) and (d). The deviation in critical points is roughly the same in configurations (a), (b), and (d), but not (c). This means that signals from probes, which are close to the plasma, enhance the robustness of fit and improve the reconstruction accuracy in all critical points. It seems that the finite edge current and high β_N ($\sim$3.7) of H-mode discharges may lead to the largest deviation. Other L- and NCS-mode discharges have $\beta_N \sim 3.5$ and ~ 3.2, respectively. A nonmonotonic q profile, characteristic of NCS-mode discharges, was not attained in runs with 3% error in signal, except with configuration (b). The different condition numbers from a few cases in Tables IV through VII result from using a different number of polynomial coefficients to reconstruct an equilibrium. Note that in the H- and NCS-mode cases with configuration (c), some of runs with 3% error in signal were not converged. This implies that information from probes and loops in configuration (c) are insufficient to reconstruct equilibrium.

V. CONCLUSION

The KSTAR PF system, which has seven up-down symmetric coil pairs and provides a flux swing of 15.5 Wb for a 20-s flattop, can satisfy strike-point and SOL flux surface constraints for both DN and SN plasmas if the X-point position is allowed to vary. Seven and nine independent circuits were used for DN and SN plasmas, respectively, to generate equilibria over the desired range of ℓ_i to β_N operating space. Superconductor allowables[7] for PF coils, which were calculated from the current at each coil, are satisfied for both DN and SN.

The RT loss requirement is automatically satisfied in KSTAR because the beam port allowance demands that the outer legs of the TF coils be located far from the plasma. The CSR loss requirement, however, configures a lower bound on the number of TF coils.[10] At least 16 TF coils are needed with reasonable height to satisfy two criteria for ripple loss. The TPX shape requires a smaller TF coil set than D and DIII-D shapes. The current design and size of the KSTAR TF coil system, with a D shape and 16 coils, satisfy both ripple criteria at the plasma and provide adequate access for NB injectors.

The EFIT code, which uses a realistic current distribution, was utilized to determine the number and position of magnetic probes and flux loops. The proposed configuration (b) in Fig. 4, based on work reported on in this paper, has 52 loops and 78 magnetic probes and allows the maximum deviation at critical points on the approximate plasma boundary to be <0.7 cm for a Gaussian-distributed 3% perturbation in signal. All four configurations were tested for L, H, and NCS modes with $\beta_N > 3.2$. The probes behind the divertor play an important role in reconstructing the plasma shape and physical

parameters of the target equilibrium. Since the deviation from target equilibrium in configuration (b), which is a full set, and (d) is roughly the same, configuration (d) has been identified as a set of the minimum number of loops and probes for KSTAR.

REFERENCES

1. G. S. LEE et al., "Design of the KSTAR Tokamak," *Proc. 20th Symp. Fusion Technology*, Marseille, France (1998); see also *Fusion Eng. Des.* (to be published).

2. J. SCHMIDT et al., *J. Fusion Energy*, **12**, 221 (1993).

3. J. L. LUXON and B. B. BROWN, *Nucl. Fusion*, **22**, 813 (1982).

4. S. C. JARDIN, N. POMPHREY, and J. DELUCIA, *J. Comp. Phys.*, **66**, 481 (1986).

5. S. P. HIRSHMAN and H. NEILSON, *Phys. Fluids*, **29**, 790 (1986).

6. S. EJIMA et al., *Nucl. Fusion*, **22**, 1313 (1982).

7. J. H. SCHULTZ, Plasma Science and Fusion Center, Massachusetts Institute of Technology, Private Communication (1998).

8. R. J. GOLDSTON, Princeton Plasma Physics Laboratory, Private Communication (1996).

9. R. J. GOLDSTON, R. B. WHITE, and A. H. BOOZER, *Phys. Rev. Lett.*, **47**, 647 (1981).

10. B. J. LEE et al., *Proc. 17th IEEE/NPSS Symp. Fusion Engineering*, p. 641, San Diego, California (1997).

11. D. K. LEE, *Comput. Phys. Commun.*, **25**, 181 (1982).

12. L. L. LAO, H. ST. JOHN, R. D. STAMBAUGH, A. G. KELLMAN, and W. PFEIFFER, *Nucl. Fusion*, **25**, 1611 (1985).

13. D. W. SWAIN and G. H. NEILSON, *Nucl. Fusion*, **22**, 1015 (1982).

14. B. J. LEE and L. L. LAO, *Bull. Am. Phys. Soc.*, **42**, 1834 (1997).

15. J. H. JHANG, Korea Basic Science Institute, Private Communication (1998).

BongJu Lee (BS, nuclear engineering, Hanyang University, Korea, 1984; MS, 1986, and PhD, 1991, nuclear engineering and engineering physics, University of Wisconsin, Madison) is a senior scientist at Korea Basic Science Institute. His research interests are magnetohydrodynamic (MHD) equilibrium and stability, divertor physics, and control of magnetic fusion confinement devices.

Neil Pomphrey (BSc, chemical physics, Edinburgh University, United Kingdom, 1972; PhD, Stirling University, United Kingdom, 1975) is a principal research physicist at the Princeton Plasma Physics Laboratory. His present interests in plasma physics include MHD theory and simulation of tokamak and stellarator plasmas.

Lang L. Lao (BS, engineering and applied science, California Institute of Technology, 1976; MSci, mechanical engineering, California Institute of Technology, 1976; PhD, nuclear engineering, University of Wisconsin, Madison, 1979) is a research scientist in the Fusion Group at General Atomics in San Diego. He is well known for his research on tokamak equilibrium and stability.